Lab on a Chip

Distributed colorimetric interferometer for mapping the pressure distribution in a complex microfluidics network

Journal:	*Lab on a Chip*
Manuscript ID	LC-ART-09-2020-000960.R2
Article Type:	Paper
Date Submitted by the Author:	31-Dec-2020
Complete List of Authors:	Zhu, Xiongfeng; University of California, Los Angeles, Mechanical and Aerospace Engineering Man, Tianxing ; University of California Los Angeles, Tan, Marvin; University of California, Los Angeles, Mechanical and Aerospace Engineering Chung, Pei-Shan ; University of California Los Angeles Teitell, Michael; University of California, Los Angeles (UCLA), Pathology and Laboratory Medicine Chiou, Pei Yu; UCLA, Department of Mechanical and Aerospace Engineering

SCHOLARONE™
Manuscripts

ARTICLE

Distributed colorimetric interferometer for mapping the pressure distribution in a complex microfluidics network

Xiongfeng Zhu,[a] Tianxing Man,[a] Xing Haw Marvin Tan,[b] Pei-Shan Chung,[b] Michael A. Teitell[bcd] and Pei-Yu Chiou*[ab]

We demonstrate a novel platform for mapping the pressure distribution of complex microfluidics networks with high spatial resolution. Our approach utilizes colorimetric interferometers enabled by lossy optical resonant cavities embedded in a silicon substrate. Detection of local pressures in real-time within a fluid network occurs by monitoring a reflected color emanating from each optical cavity. Pressure distribution measurements spanning a 1 cm^2 area with a spatial resolution of 50 μm have been achieved. We applied a machine learning-assisted sensor calibration method to generate a dynamic measurement range from 0 to 5.0 psi, with 0.2 psi accuracy. Adjustments to this dynamic measurement range are possible to meet different application needs for monitoring flow conditions in complex microfluidics networks, for the timely detection of anomalies such as clogging or leakage at their occurring locations.

Introduction

Microfluidics, which emerged in the early 1980s, is now widely used in academic research studies and in biotechnology industry applications. Lab-on-a-chip technologies have guided the development of devices that integrate multiple laboratory functions, such as sample treatment and chemical detection, on a single wafer to achieve automation, high-throughput, and rapid processing.[1,2] Key applications include DNA sequence analysis,[3,4] biomolecule synthesis,[5] drug discovery,[6–8] studies of living cell systems[9–15] and point-of-care disease diagnostics[16,17]. With microfluidics manufacturing becoming more mature, highly integrated devices can now be produced at low-cost.[18,19] When microfluidics networks scale up, especially for systems involving pumps[20] and valves,[21,22] a critical need emerges for monitoring the system to check for working conditions at different device locations. For large-scale, continuous-flow systems, it becomes especially crucial to monitor flow conditions and identify operation anomalies such as clogging[23,24] and leakage[25] in real time to provide opportunities for timely mitigation, thereby ensuring smooth operation.

Hydraulic pressure is one of the most essential parameters in all microfluidics devices since it is the driving force of fluid flow in every region of a chip.[22] Real-time mapping of local hydraulic pressure distributions throughout a large area with high spatial resolution would facilitate the future design of large-scale, complex, and interconnected microfluidics networks and also provide an in-situ monitoring function to check operating conditions of current chips.

Traditional external pressure transducers are not easily compatible with microfluidics systems due to their bulky sizes.[26] Local pressure measurements are typically through external tubing connections, and parallel measurements are impractical because of the limited space available on a microfluidics chip.[27,28] Few approaches exist to provide distributed pressure measurement functions.[29–35] Electrical methods such as an electro-fluidic circuit[29,31] or a microflotronic film[30] utilize pressure-induced structure deformation and corresponding electrical property changes to sense the pressure in microfluidics channels. These methods, however, suffer from low spatial resolution because of the need for large footprint-sized sensing units to ensure sensitivity. Optical methods that rely on monitoring the pressure-induced movement of liquid-air[32] or liquid-liquid[33] interfaces have also been proposed. A major drawback of these approaches is the need to modify existing fluidics networks to introduce such interfaces, which greatly complicates the design, fabrication, and operation of microfluidics devices. An optofluidic membrane interferometer[34] can provide high sensitivity measurements of on-chip channel pressure through imaging the interference fringe patterns formed at an optical cavity. To ensure detection sensitivity, high-resolution optical images that typically contain tens of thousands of imaging pixels are

a. Department of Mechanical and Aerospace Engineering, University of California, Los Angeles, Los Angeles, California, USA. E-mail: peiyu@g.ucla.edu.
b. Department of Bioengineering, University of California, Los Angeles, Los Angeles, California, USA.
c. Molecular Biology Institute, Department of Pathology and Laboratory Medicine, Department of Pediatrics, University of California, Los Angeles, California 90095, USA.
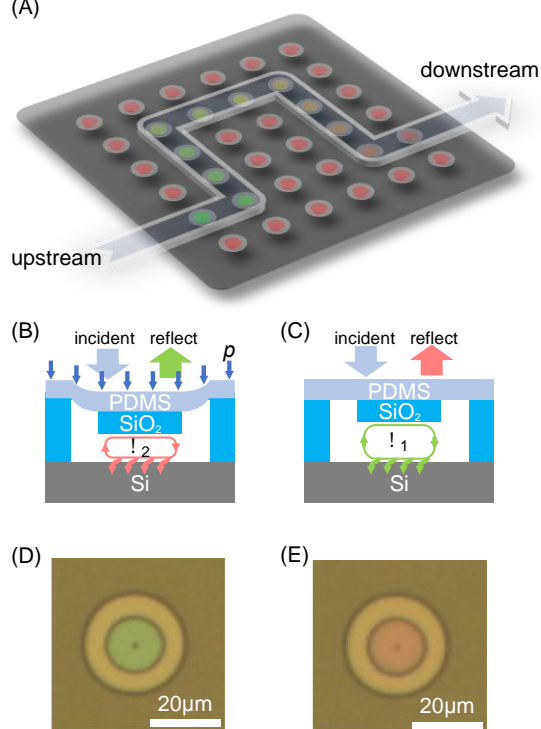d. Johnsson Comprehensive Cancer Center, University of California, Los Angeles, California 90095, USA.

required for a sensing unit, which limits the density of sensing units for deployment on a chip.

Here, we present a new distributed pressure-sensing

Fig. 1 A distributed pressure-sensing platform based on a colorimetric interferometer array. (A) Schematic of a pressure-sensing platform based on a colorimetric interferometer array. Local hydrodynamic pressure in a complex fluidics network is obtained in real-time by detecting the reflected light color from a corresponding optical cavity. (B)(C) Two schematics of the cross-section of an individual sensor unit. The unit consists of a thin PDMS membrane that deforms under fluid pressure. The SiO_2 mirror suspended below the membrane and the Si substrate forms an air cavity that functions as a lossy optical resonator. When the fluid pressure above the PDMS membrane changes, the air gap spacing also changes to result in a shift of the reflected optical spectrum. Through detecting the color composition of each cavity, the local fluid pressure above the mirror is measured. (D)(E) Example microscopy images detected from two sensor units along a fluid channel, one at the upstream high-pressure region (green color) and the other at the downstream low-pressure region (red color).

platform based on colorimetric interferometry that can extract pressure-mapping information from complex microfluidics chips with high spatial resolution in a large cross-sectional area (Fig. 1A). Our platform integrates with microfluidics networks of arbitrary shapes without a need to modify the original microfluidics structure design. Channel pressure at different locations is detected by monitoring the reflected color composition of corresponding mirrors through a common optical microscope (Fig. 1B and 1C). Each pressure sensing unit consists of a lossy optical resonant cavity formed by a thin air gap sandwiched between a transparent silicon dioxide mirror suspended on an elastic membrane and a reflective silicon substrate. When the local fluid pressure applied on a mirror changes, it changes the air gap thickness, the light interference

condition, and the reflected color composition (Fig. 1D and 1E).

Methods

Device fabrication

The device is fabricated using a combination of standard silicon-based microfabrication and PDMS-based heterogeneous integration processes.[36] It can be summarized into three major steps: (1) A thin PDMS film is prepared by spin coating (4000rpm, 5min) and baked inside an oven at 65 ^{o}C until cure to achieve a final thickness of 6 μm. This PDMS film is laterally peeled and attached temporarily onto a hybrid glass-PDMS buffer. (2) A 1.5 μm thick thermally grown silicon dioxide layer is patterned into a disk array and the silicon substrate underneath is isotropically etched to form thin needle-shaped anchors under these disks. These silicon dioxide disks are then permanently bonded to a thin PDMS film through oxygen plasma treatment (80 W, 500 mT, 30 s) and oven baked for 2 hours at 65 ^{o}C. Then, the whole sample is immersed in a water/acetone (1:1 v/v ratio) ultrasonic bath to break the silicon anchors and transfer the disk array. (3) Another silicon substrate with the same thickness of thermal oxide goes through another step of plasma-enhanced chemical vapor deposition (PECVD) to add an extra 550 nm oxide thickness to define the initial air gap spacing. An array of wells is etched out to accommodate the oxide disk array. Finally, this substrate is align-bonded with the thin PDMS film mounted with an array of oxide disks to form the optical cavities, and finally, the hybrid buffer is peeled off. The device can go through an optional prolonged oxygen plasma treatment (80 W, 500 mT, 7 mins) to create a thin silica-like layer on top of the PDMS surface to help block the penetration of water vapor to extend the device operation lifetime under a high hydraulic pressure environment.[37,38] More fabrication details are illustrated in Fig. S1†.

Imaging setup

An upright microscope (Zeiss Axio Scope A1) is used to image the device with a 10× objective lens (N.A. 0.25). The broadband white light illumination source is from a halogen lamp (HAL 100) attached to the microscope. A color CMOS camera sensor (Grasshopper GS3-U3-41C6C-C) is attached to the microscope to capture images for analysis. The camera is set to have a fixed exposure time of 0.35 ms. All image preprocessing functions on this camera are turned off, and exported images are in the raw file format to prevent information loss.

FDTD simulation and numerical calculation

The numerical simulation is conducted using a commercial FDTD software (RSoft) based on a single unit of optical cavity. The model is simplified to a 2D cross-sectional study with periodic boundary conditions on two sides. Material properties are set accordingly to the built-in refractive index library. An emitter sends optical waves vertically into the cavity and a receiver behind the emitter measures the reflected power. We run parametric sweep on the wavelength of light and air gap thickness to generate the reflectance spectra in Fig. 2A. To compute the color transition in Fig.

2D, we adopted the illumination spectrum of the halogen lamp (Fig. S2†) measured by a commercial spectrometer (Ocean Optics HL-2000-HP), and the camera sensor color sensitivity spectra (Fig. S3†) in the specification manual provided by the manufacturer.

Pressure and flow rate control

A precision pressure regulator (Marsh Bellofram 510PI0G015P0100 Digital Pressure Regulator) is used to control the pressure output during calibration experiments. The regulator takes a 20 psi compressed air as input and regulates the pressure output within the range of 0 to 15 psi based on the voltage control signal from 0 to 10 V using a DC power supply (Gw Instek GPS-3303), and has a built-in digital display for pressure readout. It can maintain a stable pressure output with < 0.1psi fluctuation using feedback control. Pressure levels from 0.2 psi to 5 psi with a step of 0.2 psi are tested. At each pressure level calibration is repeated multiple times by taking 45 consecutive images with 100 ms interval and fixed 0.35 ms exposure time.

A syringe pump (Harvard PHD 2000 Infusion) is used to control the flow rate during pressure mapping demonstration. A syringe (BD 10 ml, Luer-Lok) filled with DI water is mounted onto the pump to supply a continuous flow into the microfluidic network through tubing connection. Various flow rates from 0.25 ml/h to 2 ml/h with a step of 0.25 ml/h are tested. After each flow rate adjustment, we wait for at least 10 mins in order to let the flow stabilize and reach steady state.[27] Then images are captured at several locations inside the microfluidic network to map out the pressure distribution. For each flow condition, the measurement is repeated multiple times by taking 45 consecutive images with 100 ms time interval and fixed 0.35 ms exposure time.

Image processing

Each measurement consists of 45 still images with minimal relative movement. We take the first frame from each measurement to find the center coordinates of pressure sensing spots of interest and assume them to remain the same for following frames. Scikit-image, an open-source image processing library for the Python programming language,[39] together with customized codes are used to extract the Hue and Saturation readings. Each color spot actually contains more than 100 pixels in the image. To improve accuracy, we don't include pixels close to object edges, and thus limit our calculations to pixels within a ring-shaped area whose inner circle is 3 pixels away from the spot center and outer circle 3 pixels away from the spot edge, leaving us about 40 pixels for each spot with plenty of redundancy. The Hue and Saturation readings for these pixels are averaged such that each spot ends up having one Hue reading and one Saturation reading in a single frame of image. Therefore 45 images provide 45 times of measurements for each pressure level calibration experiment. Since there are 25 pressure levels sampled between 0.2 psi to 5 psi every 0.2 psi, we append these measurements together to form a calibration dataset consisting of 1125 data points in total and provide the basis for regression analysis of one measurement spot. Each calibration data point has the Hue and the Saturation readings, and is

associated/labeled with a pressure level somewhere between 0.2 psi to 5 psi.

Regression analysis and pressure prediction

For each measurement spot we have 1125 calibration data points based on which we perform a regression analysis between the color attributes and the pressure level as a way of nonlinear sensor calibration. Fig. 4A serves as the data visualization and inspires us to try out two regression models: parametric polynomial regression and non-parametric kNN regression. Scikit-learn, an open-source statistical learning library for the Python programming language,[40] is used for the regression analysis and establish the relationship between color attribute readings and the pressure level. To select the optimal parameters, namely the highest degree in polynomial regression and the number of neighbors in kNN regression, we used leave-one-out cross-validation (LOOCV) to evaluate the model performance with mean absolute error as the evaluation metric. After establishing the relationship and saving the model, we are able to make pressure prediction based on the color of a measurement spot by extracting the Hue and Saturation readings as inputs and correlating them to a pressure level.

Results and discussion
Working principle
The optical wavelength-selective reflection response of an air cavity originates from its role as a lossy optical resonator. Light rays reflected at the SiO_2/air interface interfere with those reflected at the air/Si interface. Little reflection is detected at the mirror when the wavelength of light satisfies the destructive interference criterion in the reflection direction

$$2t = n\lambda, n = 1, 2, 3, \dots$$

$$\lambda = 2t, t, \frac{2}{3}t, \dots$$

where t is the air gap thickness and λ is the wavelength of light. Light of these wavelengths enter the cavity, bounce back and forth, and eventually become absorbed by the silicon substrate. However, when the wavelength of light satisfies the constructive interference criterion,

$$2t = \left(n + \frac{1}{2}\right)\lambda, n = 0, 1, 2, \dots$$

$$\lambda = 4t, \frac{4}{3}t, \frac{4}{5}t, \dots$$

, strong light reflection occurs. These wavelengths of light constitute the final color spectrum captured by a camera from each corresponding cavity. Numerical simulation using the finite-difference time-domain (FDTD) method calculates the reflectance spectra from an optical cavity in the visible light range (Fig. 2A). In our device, the initial air gap thickness t_0 was designed to be ~ 600 nm, and the target operation range was set to be less than 300nm for optimal operation in the visible

ARTICLE

light range. We selectively plotted the reflectance spectra for gaps at 500nm, 420nm, and 360nm (Fig. 2B). Wavelengths at which minimum reflectance occurs are close to 500nm, 420nm and 720nm, respectively, which aligns with the above analytical analysis based on light interference principles.

To calculate the reflection spectrum detected by the imaging system, we consider three main factors, the light source spectrum, the reflection spectrum from an air cavity, and the reception of the image sensor. To compute the colors perceived by the image sensor, we first adopt the RGB color model by calculating the value of each component with the following set of equations

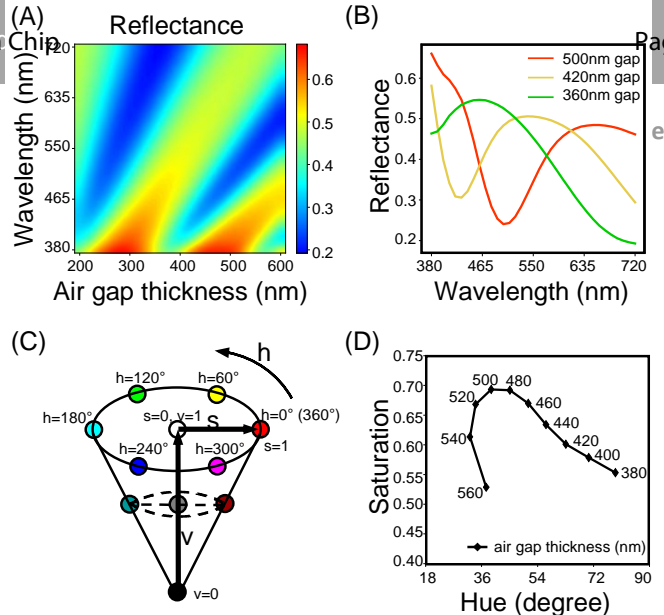$$R = \int_0^\infty I(\lambda)S(\lambda)r(\lambda)d\lambda$$

$$G = \int_0^\infty I(\lambda)S(\lambda)g(\lambda)d\lambda$$

$$B = \int_0^\infty I(\lambda)S(\lambda)b(\lambda)d\lambda$$

where $I(\lambda)$ is the illumination spectrum of the light source measured by a spectrometer (Fig. S2†), $S(\lambda)$ is the reflectance spectrum of our device obtained from the FDTD numerical simulation, and $r(\lambda), g(\lambda), b(\lambda)$ are the spectral sensitivities of red, green, and blue pixels of the image sensor provided by the manufacturer (Fig. S2†). We sampled the spectral data points every 20 nm and calculated the RGB intensities perceived by the image sensor at different air gap thicknesses. The results, however, indicated that the change of red (R) and green (G) channels closely follow each other, and the blue (B) channel signal is weak. Furthermore, the readings of RGB channels are subject to scale simultaneously when the light intensity and exposure time fluctuates. These factors strongly suggest that the RGB color index is not ideal for quantifying the relationship between the reflection spectra and air gap spacing. Therefore, we turned to an alternative HSV (Hue, Saturation, Value) color index that decouples brightness (Value) from color (Hue and Saturation) attributes (Fig. 2C). In the HSV color index, Hue is the attribute of human perceived color, such as red, yellow, green, and blue. The Hue parameter is typically represented by the angle degree of a rainbow wheel. For example, red is at zero degrees, green at 120 degrees, and blue at 240 degrees. Saturation is the attribute representing pureness of a color, and Value is the attribute representing the brightness of a color.[41] The Hue and Saturation attributes provide the spectrum components of a color, and therefore are ideal parameters for characterizing the relationship between the spectrum change and the air gap spacing. The indices of the RGB model can be converted to the HSV model based on the following formula:

$$H' = \begin{cases} (\dfrac{G-B}{max_{channel}-min_{channel}} + 0)/6; \text{if max} = R^* \\ (\dfrac{B-R}{max_{channel}-min_{channel}} + 2)/6; \text{if max} = G \\ (\dfrac{R-G}{max_{channel}-min_{channel}} + 4)/6; \text{if max} = B \end{cases}$$

$*$ if H' is less than 0 then add 1 to H'

Fig. 2 Working principle. (A) Numerical simulation of the reflectance spectra in the visible light range as a function of air gap thickness. (B) The reflectance spectra at three selected air gap thicknesses extracted from (A) to show that the wavelengths at which minimum reflection occurs matches the analytical analysis results. (C) Cone plot of the HSV (Hue, Saturation, Value) color model. Different perceived colors (red, blue, green, etc.) are represented by different degrees of Hue. Different levels of colorfulness are represented by Saturation on a scale from 0 to 1. The brightness of a color is represented by the parameter Value. (D) Plot of reflected colors in terms of their Saturation and Hue values at different air gap thickness. We calculate colors by integrating the product of light source intensity, device reflectance, and camera pixel sensitivity over the range of the visible light wavelength spectrum.

$$H = H' \times 360°$$

$$S = \frac{max_{channel} - min_{channel}}{max_{channel}}$$

$$V = max_{channel}$$

After converting to the HSV color model, we observed that the change of the Value channel is much smaller than the Hue or Saturation channels when the air gap thickness varies. In addition, the Hue and Saturation channels are more resistant to potential light intensity fluctuations. Both of these desirable features corroborate our choice to use the HSV model and examine the Hue and Saturation channels for quantifying the relationship between color composition and air gap thickness. In Fig. 2D is a simulation result showing the relationship between air gap thickness and Saturation and Hue values. There is a trend of clockwise progression on the Hue-Saturation plot when the air gap thickness decreases from 560nm to 380nm.

Machine learning-assisted multivariant nonlinear sensor calibration

ARTICLE

To validate the results predicted from the above theoretical analysis and numerical simulation, we performed calibration experiments with a fabricated device under a microscope (Fig. 3A). A microfluidics channel was bonded on top of the device and filled with water as the pressure-transmitting medium. Pressure was
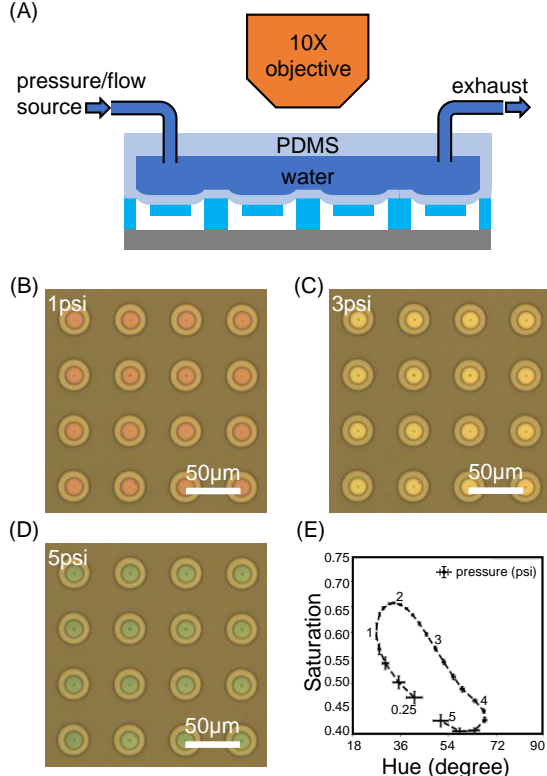

Fig. 3 Pressure calibration. (A) Schematic of the experimental setup for calibrating the relationship between pressure and air-gap sensor color response. A microfluidics channel was bonded on top of our colorimetric pressure- sensing platform for this calibration test. The assembled platform was placed under a standard upright microscope with a 10× objective lens for imaging. For pressure calibration the exhaust outlet was sealed to form a closed chamber. (B, C, D) Microscopic images showing different colors captured at different pressure levels. (E) Experimentally measured colors at different pressure levels are plotted in terms of their Saturation and Hue values. Each data point on the plot is the average result of 27 sensing units. Each one is measured 45 times at each pressure level with error bars representing the standard deviation.

supplied by a pressure regulator with built-in digital calibration. The regulator provides a stable pressure output with fluctuations less than 0.1 psi. We sampled the pressure level from 0 to 5 psi with 0.2 psi intervals. Each pressure level measurement was repeated 45 times. Images were captured using a color CMOS sensor at different pressure levels to demonstrate the color transition effect (Fig. 3B – 3D). The Hue and Saturation values from the pixels of a corresponding cavity were extracted and averaged. The results measured at different pressure levels were compiled into one plot (Fig. 3E). The trend of clockwise progression on the Hue-Saturation plot when the pressure level increases, which causes the air gap to decrease, matches well with our simulation results shown in Fig. 2D.

In order to establish the correlation between Hue and Saturation readings and the actual pressure level in the

microfluidics channel, we formulate the problem as a multivariate nonlinear sensor calibration using the experimental calibration data (Fig. 4A). Statistical learning methods have been previously applied to such nonlinear sensor calibration problems.[42–45] Here, we explore the applications of two models, (1) polynomial regression and (2) k-nearest neighbors (kNN) regression, to fit the experimental data and build a model that can reliably predict the pressure level based on Hue and Saturation readings. Polynomial regression, as a commonly used parametric curve fitting method, fits a nonlinear relationship between independent variable X and dependent variable Y by statistically estimating Y to be a linear combination of X and its higher-degree terms. The goodness of fitting largely depends on the wise choice of X and proper order of the highest degree. Seeing the clear clockwise progression from visualizing data points in a 2D plot with respect to the Hue and Saturation readings (Fig. 3E), we first calculated the mean for all Hue and Saturation readings and used that center point as a new origin. Then, the vector of a data point is defined as the one connecting the new origin and the data point itself. The vector of the very first calibration data with the lowest pressure level was taken as a reference vector, and we chose X to be the clockwise directional angle between any data vector and the reference vector. With the proper choice of the highest degree, we can fit relatively well on the whole set of calibration data (Fig. 4B).

The K-nearest neighbors regression, which is a non-parametric technique,[46] predicts the value of Y based on a similarity measure between a new measurement and all the existing calibration data. Accuracy is usually affected by the choice of distance function as a measure of similarity, and the choice of how many neighbors examined. We chose the Euclidean distance between data points as the similarity measurement and achieved a fitting even better than the polynomial regression method for the whole calibration data (Fig. 4C). To further evaluate the generalized model performance when encountering new measurements in the future and prevent overfitting, we performed leave-one-out cross-validation (LOOCV)
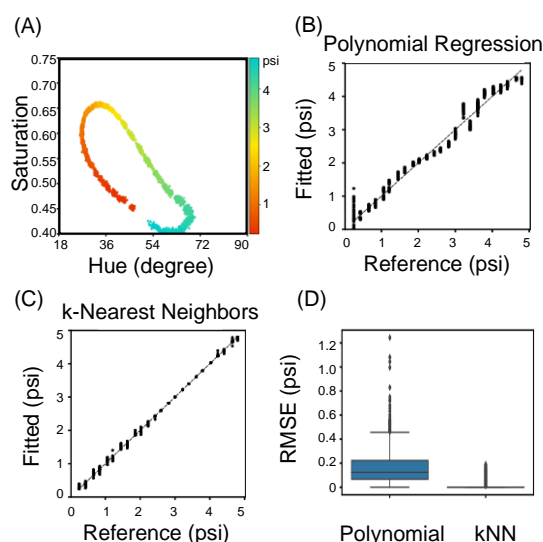

Fig. 4 Nonlinear sensor calibration with experimental data. (A) Plot of Saturation and Hue readings corresponding to pressure levels from 0 to 5 psi. (B) The goodness of fitting by applying the polynomial regression to the dataset. The fitted value is given by the model based on Saturation and Hue readings as input and plotted against the actual value as reference. (C) The goodness of fitting by applying the kNN regression to the dataset. (D) Generalized model performance evaluated by using the leave-one-out cross-validation method. Each point represents the difference between the actual pressure of one test and the predicted pressure.

Please do not adjust margins
Lab on a Chip
Page 6 of 9

using the calibration dataset (Fig. 4D). The kNN regression showed superior performance with lower median error and narrower error variation. The absolute error was less than 0.2 psi as shown by the outlier with the largest error. With a denser pressure calibration interval used, the error from the kNN regression model can ultimately reduce down to the precision of the pressure regulator used for calibration.

Pressure mapping inside a complex microfluidics network

Using the prediction model built by the kNN regression method, we mapped the Hue and Saturation values to the pressure applied on top of an air cavity. As a potential application, we apply this distributed pressure-sensing platform to map the pressure distribution inside a complex microfluidics network (Fig. 5A). We fabricated the microfluidic channels using a soft lithography method and bonded it to our platform. The microfluidics network spans an area of 8 mm × 5 mm and is covered by more than 10,000 pressure-sensing units evenly distributed with a 50 μm pitch. A flow-rate-controlled syringe pump was used to drive water through the network at different flow rates. After flow stabilization, color images were captured at the inlet, middle and outlet areas of the network in order to map pressures in these zones. Since pressure drops from the upstream inlet to the downstream outlet in a continuous flow, different regions exhibit different colors (Fig. 5A). At each location, we repeated the measurements by taking multiple image frames under steady state flow conditions. Each image contained more than one hundred pressure-sensing spots. As a
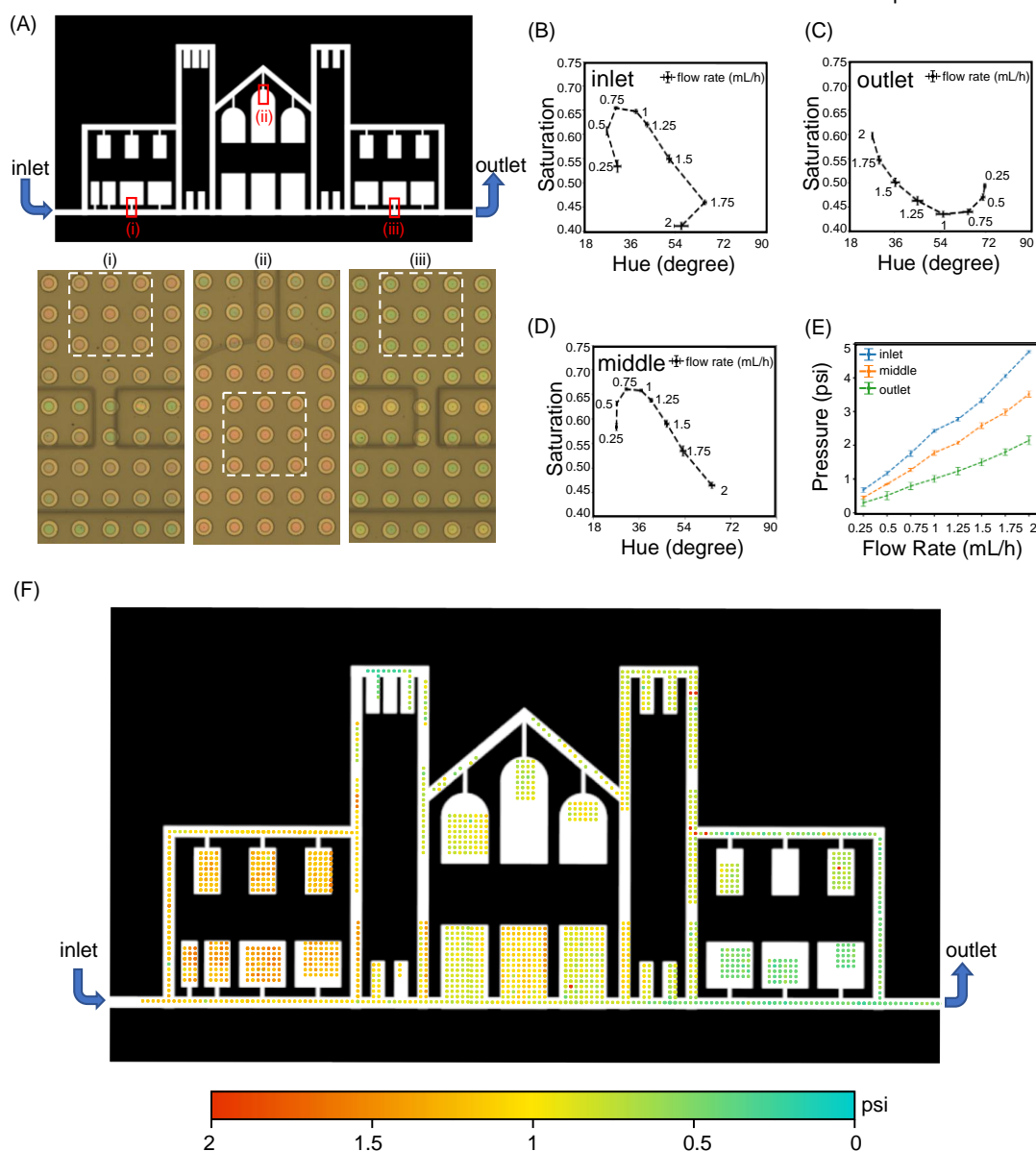
Fig. 5 Mapping pressure distribution in a complex microfluidics network. (A) Design of a complex microfluidics network spanning a 8 mm × 5 mm cross-sectional area. The example images are for a flow rate of 0.25 ml/h at (i) inlet, (ii) middle, and (iii) outlet positions of the microfluidics network. These three regions show different colors that represent different pressure levels. (BCD) Hue-Saturation plots for flow rates between 0.25 and 2 ml/h at inlet, middle, and outlet network locations. Each data point represents measurements from 9 sensing units at each location. (E) Measured relationships between pressure and flow rates at inlet, middle, and outlet network locations. Each data point represents data from 9 sensing units at each location. (F) Pressure distribution at 0.8 ml/h flow rate mapped throughout the entire microfluidics network.

demonstration, we cropped the images and evaluated the same spot in each area under different flow rates. The Hue and Saturation readings from these spots were extracted and plotted (Fig. 5B – 5D). With the previous calibration data and kNN regression modeling, we measured the pressure at different locations under different flow rates (Fig. 5E). Pressure drops between any two spots can be simply calculated and used to monitor flow conditions. When the change is from an overall flow rate adjustment, we expect the pressure drop at different regions to change simultaneously and proportionally. However, when the change is from anomalies, such as clogging or leakage at some locations, our distributed multispot pressure-sensing platform should detect regions showing an abnormality by plotting the pressure distribution map. Fig. 5F shows an example of a pressure distribution map for an entire complex microfluidics network used in our study. The experimental result agrees well with the pressure distribution obtained from numerical studies as shown in Fig. S4†.

Discussion

A dynamic, real-time map of pressure distribution inside a microfluidics network can provide vital information about network operating conditions. Although there has been effort to develop microfluidics pressure sensors, a platform providing high spatial resolution pressure mapping for large-scale microfluidics networks is not yet available. Here, we demonstrate a distributed color interferometry-based pressure-sensing platform with more than 10,000 pressure sensing spots spanning a 1 cm^2 cross-sectional area with 50 μm spatial resolution. We used a 10× objective lens for imaging. Each silicon dioxide mirror provides ~ 40 imaging pixels in a total image. Silicon dioxide has a Young's Modulus of 70 GPa, which is nearly 5 orders of magnitude larger than the surrounding PDMS structure. On one hand, the supporting silicone dioxide from the substrate firmly anchors PDMS film and effectively decouples the mechanical responses of neighboring sensing spots when separated 50 μm apart (Fig. S5†). On the other hand, each silicone dioxide mirror remains rigid and flat during the pressure-sensing process. All optical pixels corresponding to an individual silicon dioxide mirror show nearly identical color compositions and change simultaneously when the PDMS membrane deforms and an air cavity changes thickness. In principle, a single optical pixel is sufficient for measurement at each spot in a microfluidics network. This suggests that concurrent monitoring of dynamic pressure changes over a large area microfluidics network is feasible with a lens for a larger field of view, as long as there is at least one optical pixel to cover each mirror.

In our platform, each mirror sensing unit functions independently as a local pressure sensor. It can provide the local pressure measurement even when neighbouring sensing units fail. Defect sensing mirrors represent dead pixels on a pressure map. If the dead pixels are sparsely distributed and if the local pressure spatial variation rate is smaller than the pixel resolution, pressure measured by neighbouring sensing units can be used to linearly fit and estimate the pressure at the missing pixels. If the defect pixels are clustered together, such fitting approaches may not work if the cluster sizes are large.

The majority defects on our platform belongs to the second type in which dead mirrors typically cluster in certain regions. Majority areas have good mirror array without dead pixels. The pressure map shown in Fig. 5(F) shows a pressure map with this type of defects. The regions with white colors are where these defect mirrors located. The overall manufacturing yield currently achieved is ~ 80%. The causes of these fabrication defects mainly come from the bonding equipment. Since the bonding process involves transferring a thin PDMS film onto any array of SiO$_2$ microwells, the tilting, the bonding pressure uniformity, and the alignment of these surfaces across a large area is critical. Further improvements of device fabrication yield can be achieved with better alignment-bonding apparatus.

We designed an operational air gap spacing to be within a range of 300-600 nm for highest color performance and transition contrast. This range of deformation should have minimal impact on flow conditions for typical microfluidic channel height spanning across tens to hundreds of microns. For the specific mechanical design in our demonstration, the measurable pressure range was between 0 ~ 5 psi. This dynamic sensing range can be tuned by changing the thickness of the PDMS membrane or adjusting its chemical composition to tune its Young's Modulus.

The demonstrated distributed pressure sensing platform can have broader applications than pressure sensing in a fluidic network. The key feature of our platform is the high-density distributed pressure sensing units. Such units do not necessarily need to integrate with a fluid channel, and can be modified for different applications. For example, if a group of single cells are properly arrayed and aligned on these pressure sensing units, by integrating a rigid and transparent mechanical stamp, it is possible to measure in parallel single cell mechanics properties through monitoring the displacement of the stamp and the corresponding displacement of each sensing unit to know the applied force and the deformation of each single cell. In another example, if a slice of tissue layer is placed on top of this distributed sensor platform and gently squeezed, the pressure sensor array can map out stress distribution to provide clues of stiffness distribution of a sheet of tissue sample.

Conclusion

We designed and demonstrated a high spatial resolution, high sensitivity, large area pressure-sensor platform. With an optimized computation framework, monitoring flow conditions inside a complex microfluidics network in real-time is possible, with fully mapped pressure distribution to detect anomalies such as clogging or leakage at any network location. As a massively parallel pressure-sensing substrate by itself, this platform may also have broad potential utility in fields outside of microfluidics, such as mechanobiology that studies the relationship between mechanical properties and biological phenomena, such as cell proliferation, growth, and differentiation.[47–50]

Conflicts of interest

There are no conflicts of interest to declare.

Please do not adjust margins
Lab on a Chip
Page 8 of 9

Journal Name

Acknowledgements

References

1   L. R. Volpatti and A. K. Yetisen, *Trends in Biotechnology*, 2014, **32**, 347–350.

2   G. M. Whitesides, *Nature*, 2006, **442**, 368–373.

3   F. Taub E., J. M. DeLEO and E. B. Thompson, *DNA*, 1983, **2**, 309–327.

4   A. Wainright, U. T. Nguyen, T. Bjornson and T. D. Boone, *ELECTROPHORESIS*, 2003, **24**, 3784–3792.

5   C.-C. Lee, G. Sui, A. Elizarov, C. J. Shu, Y.-S. Shin, A. N. Dooley, J. Huang, A. Daridon, P. Wyatt, D. Stout, H. C. Kolb, O. N. Witte, N. Satyamurthy, J. R. Heath, M. E. Phelps, S. R. Quake and H.-R. Tseng, *Science*, 2005, **310**, 1793–1796.

6   P. S. Dittrich and A. Manz, *Nat Rev Drug Discov*, 2006, **5**, 210–218.

7   J. Pihl, M. Karlsson and D. T. Chiu, *Drug Discovery Today*, 2005, **10**, 1377–1383.

8   T. Man, X. Zhu, Y. T. Chow, E. R. Dawson, X. Wen, A. N. Patananan, T. L. Liu, C. Zhao, C. Wu, J. S. Hong, P.-S. Chung, D. L. Clemens, B.-Y. Lee, P. S. Weiss, M. A. Teitell and P.-Y. Chiou, *ACS Nano*, 2019, **13**, 10835–10844.

9   P. J. Hung, P. J. Lee, P. Sabounchi, R. Lin and L. P. Lee, *Biotechnol. Bioeng.*, 2005, **89**, 1–8.

10 A. R. Wheeler, W. R. Throndset, R. J. Whelan, A. M. Leach, R. N. Zare, Y. H. Liao, K. Farrell, I. D. Manger and A. Daridon, *Anal. Chem.*, 2003, **75**, 3581–3586.

11 A. A. Werdich, E. A. Lima, B. Ivanov, I. Ges, M. E. Anderson, J. P. Wikswo and F. J. Baudenbacher, *Lab Chip*, 2004, **4**, 357–362.

12 B. G. Chung, L. A. Flanagan, S. W. Rhee, P. H. Schwartz, A. P. Lee, E. S. Monuki and N. L. Jeon, *Lab Chip*, 2005, **5**, 401–406.

13 X. Zhu, K.-W. Tung and P.-Y. Chiou, *Applied Physics Letters*, 2017, **111**, 143506.

14 A. M. Taylor, S. W. Rhee, C. H. Tu, D. H. Cribbs, C. W. Cotman and N. L. Jeon, *Langmuir*, 2003, **19**, 1551–1556.

15 G. M. Walker, J. Sai, A. Richmond, M. Stremler, C. Y. Chung and J. P. Wikswo, *Lab Chip*, 2005, **5**, 611–618.

16 C. M. Pandey, S. Augustine, S. Kumar, S. Kumar, S. Nara, S. Srivastava and B. D. Malhotra, *Biotechnology Journal*, 2018, **13**, 1700047.

17 S. K. Sia and L. J. Kricka, *Lab Chip*, 2008, **8**, 1982–1983.

18 A. Manz, D. J. Harrison, E. M. J. Verpoorte, James. C. Fettinger, A. Paulus, H. Lüdi and H. M. Widmer, *Journal of Chromatography A*, 1992, **593**, 253–258.

19 T. Thorsen, S. J. Maerkl and S. R. Quake, *Science*, 2002, **298**, 580–584.

20 D. J. Laser and J. G. Santiago, *J. Micromech. Microeng.*, 2004, **14**, R35–R64.

21 D. B. Weibel, M. Kruithof, S. Potenta, S. K. Sia, A. Lee and G. M. Whitesides, *Anal. Chem.*, 2005, **77**, 4726–4733.

22 J. W. Hong and S. R. Quake, *Nat Biotechnol*, 2003, **21**, 1179–1183.

23 Y. Yoon, S. Kim, J. Lee, J. Choi, R.-K. Kim, S.-J. Lee, O. Sul and S.-B. Lee, *Sci Rep*, 2016, **6**, 1–8.

24 E. Dressaire and A. Sauret, *Soft Matter*, 2016, **13**, 37–48.

25 Kai Hu, Feiqiao Yu, Tsung-Yi Ho and K. Chakrabarty, *IEEE Trans. Comput.-Aided Des. Integr. Circuits Syst.*, 2014, **33**, 1463–1475.

26 Y. Chen, H. N. Chan, S. A. Michael, Y. Shen, Y. Chen, Q. Tian, L. Huang and H. Wu, *Lab Chip*, 2017, **17**, 653–662.

27 N. Mavrogiannis, M. Ibo, X. Fu, F. Crivellari and Z. Gagnon, *Biomicrofluidics*, 2016, **10**, 034107.

28 J. R. Lake, K. C. Heyde and W. C. Ruder, *PLOS ONE*, 2017, **12**, e0175089.

29 M.-C. Liu, H.-C. Shih, J.-G. Wu, T.-W. Weng, C.-Y. Wu, J.-C. Lu and Y.-C. Tung, *Lab on a Chip*, 2013, **13**, 1743.

30 R. Li, B. Nie, P. Digiglio and T. Pan, *Adv. Funct. Mater.*, 2014, **24**, 6195–6203.

31 E. P. Kartalov, G. Maltezos, W. F. Anderson, C. R. Taylor and A. Scherer, *J Appl Phys*, 2007, **102**, 84909–849094.

32 N. Srivastava and M. A. Burns, *Lab on a Chip*, 2007, **7**, 633.

33 N. S. Suteria, M. Nekouei and S. A. Vanapalli, *Lab on a Chip*, 2018, **18**, 343–355.

34 W. Song and D. Psaltis, *Biomicrofluidics*, 2011, **5**, 044110.

35 K. Hosokawa, K. Hanada and R. Maeda, *J. Micromech. Microeng.*, 2001, **12**, 1–6.

36 X. Wen, B. Wang, S. Huang, T. "Leo" Liu, M.-S. Lee, P.-S. Chung, Y. T. Chow, I.-W. Huang, H. G. Monbouquette, N. T. Maidment and P.-Y. Chiou, *Biosensors and Bioelectronics*, 2019, **131**, 37–45.

37 S. Béfahy, P. Lipnik, T. Pardoen, C. Nascimento, B. Patris, P. Bertrand and S. Yunus, *Langmuir*, 2010, **26**, 3372–3375.

38 S. H. Tan, N.-T. Nguyen, Y. C. Chua and T. G. Kang, *Biomicrofluidics*, , DOI:10.1063/1.3466882.

39 S. van der Walt, J. L. Schönberger, J. Nunez-Iglesias, F. Boulogne, J. D. Warner, N. Yager, E. Gouillart and T. Yu, *PeerJ*, 2014, **2**, e453.

40 F. Pedregosa, G. Varoquaux, A. Gramfort, V. Michel, B. Thirion, O. Grisel, M. Blondel, P. Prettenhofer, R. Weiss, V. Dubourg, J. Vanderplas, A. Passos, D. Cournapeau, M. Brucher, M. Perrot and É. Duchesnay, *Journal of Machine Learning Research*, 2011, **12**, 2825–2830.

41 M. D. Fairchild, *Color Appearance Models*, John Wiley & Sons, 2005.

42 B. M. Nikolova, G. T. Nikolov and M. H. Todorov, 2009, 4.

43 W. P. Carey and S. S. Yee, *Sensors and Actuators B: Chemical*, 1992, **9**, 113–122.

44 S. Sekulic, M. B. Seasholtz, Z. Wang, B. R. Kowalski, S. E. Lee and B. R. Holt, 11.

45 D. H. Hagan, G. Isaacman-VanWertz, J. P. Franklin, L. M. M. Wallace, B. D. Kocar, C. L. Heald and J. H. Kroll, *Atmospheric Measurement Techniques*, 2018, **11**, 315–328.

46 N. S. Altman, *The American Statistician*, 1992, **46**, 175–185.

47 P.-H. Wu, D. R.-B. Aroush, A. Asnacios, W.-C. Chen, M. E. Dokukin, B. L. Doss, P. Durand-Smet, A. Ekpenyong, J. Guck, N. V. Guz, P. A. Janmey, J. S. H. Lee, N. M. Moore, A. Ott, Y.-C. Poh, R. Ros, M. Sander, I. Sokolov, J. R. Staunton, N. Wang, G. Whyte and D. Wirtz, *Nature Methods*, 2018, **15**, 491–498.

48 B. F. Kennedy, P. Wijesinghe and D. D. Sampson, *Nat Photon*, 2017, **11**, 215–221.

49 I. Pushkarsky, P. Tseng, D. Black, B. France, L. Warfe, C. J. Koziol-White, W. F. Jester, R. K. Trinh, J. Lin, P. O. Scumpia, S. L. Morrison, R. A. Panettieri, R. Damoiseaux and D. D. Carlo, *Nature Biomedical Engineering*, 2018, **2**, 124.

ARTICLE

50   C. Wu, X. Zhu, T. Man, P.-S. Chung, M. A. Teitell and P.-Y. Chiou, *Lab Chip*, 2018, **18**, 3074–3078.